MnO₂/CdS/N-doped Graphite Nanocomposite for High-Performance Supercapacitors

Liang Chen, Yinze Zuo, Yu Zhang and Yanmin Gao[*]

School of Materials Science and Engineering, Jiangsu University of Science and Technology, Jiangsu, Zhenjiang 212003, China
[*]E-mail: gymjust@126.com

To improve the electrochemical performance of supercapacitors, the reaction mechanism and structural design should be examined simultaneously. In this work, an N-doped graphite (NG) layer was self-assembled directly on a Ni matrix and acted as an active interlayer between the current collector and the active material. For the first time, ultrafine CdS nanoparticles were synthesized on an NG layer directly as the electrode active material. Subsequently, MnO_2 nanowires penetrated the gaps between the CdS particles and tightly anchored the CdS nanoparticles on the surface of the NG. The presence of the MnO_2 nanowires was demonstrated to prompt charge transfer into the interior CdS and facilitate the redox reaction at the MnO_2-CdS@NG electrode. In addition, due to the synergy of the N-doped interlayer and the novel reinforced structure, the chemical activity and cycling stability were improved. From the electrochemical measurements, the specific capacitance of the MnO_2-CdS@NG electrode was 1497 F g^{-1} at the current density of 2 A g^{-1}. In addition, the MnO_2-CdS@NG//rGO asymmetric supercapacitor exhibited a superior energy density (33.8 W h kg^{-1} at a power density of 776 W kg^{-1}) and a great cycling stability (87% at a current density of 10 A g^{-1} for 5000 cycles).

1. INTRODUCTION

Due to rapid fossil fuel consumption and serious environmental pollution, clean and renewable energy storage devices are in demand. Supercapacitors (SCs) have gained great attention due to their superior electrochemical properties, such as fast charge-discharge rate, high power output and long cycling stability [1-3]. To date, SCs have been widely used in hybrid vehicles, military weapons and industrial equipment. However, the further application of SCs is limited by their energy density, which is lower than that of rechargeable batteries. To solve this problem, numerous active electrode materials

have been investigated for their performance as SCs. Generally, three main types of active materials can be distinguished: carbon materials, metal oxides and conducting polymers [4-7].

Recently, metal sulphides have demonstrated the ability to undergo a reversible redox reaction in alkaline electrolytes. They also exhibit greater electrical conductivity, higher specific capacitance and longer cycling stability than metal (hydro-) oxides [8-10]. The present correlative studies mainly focus on elements like Mn, Co, Ni, Cu and Mo, and hence, it is necessary to investigate other metal elements to develop novel electrode materials. Cd has been widely known for its use in cadmium nickel batteries, in which a Cd-based electrode contributes a high energy density and great rate stability. Therefore, it is very desirable to explore the performance of CdS as an electrode active material for SCs. Xu and co-workers have synthesized porous CdS on a Ni foam, which exhibited a specific capacitance of 909 F g^{-1} at 2 mA cm^{-2} [11]. Zhang and co-workers reported RGO/CdS hydrogels for SCs, which showed a specific capacitance of 300 F g^{-1} at 5 mV s^{-1} [12]. Since CdS is a group II-VI semiconductor material whose electronic properties are significantly affected by modification, there is still much room to improve the capacitive performance of CdS.

Because of their high conductivity, great flexibility and large surface area, carbonaceous networks such as graphene, CNTs and carbon microfibres have been regarded as ideal substrates for the synthesis of active materials [13-19]. Furthermore, the combination of active materials with carbonaceous networks will improve the cycling stability. However, the adhesive used to fabricate the electrode increases the charge-transfer resistance. To avoid the use of an adhesive, in this work, an ultrathin N-doped graphite (NG) layer was directly synthesized for the first time on a Ni matrix by the precipitation of a solid dissolved carbon source. Then, ultrafine CdS nanoparticles were synthesized on the NG layer and stabilized by MnO_2 nanowires that penetrated the gaps between the CdS particles. This MnO_2-CdS@NG electrode has not previously been reported. Due to the synergy of the N-doped interlayer and the novel reinforced structure, the chemical activity and cycling stability of the MnO_2-CdS@NG electrode were improved. In addition, the MnO_2-CdS@NG//rGO asymmetric supercapacitor exhibited a superior electrochemical performance for practical applications.

2. EXPERIMENTAL

2.1. Synthesis of the N-doped graphite layer

Polyacrylonitrile fibres (1 g) and Ni foams (1 × 1.5 cm) were put together into a tube furnace. The polyacrylonitrile fibres (PAN:PMMA = 85:15) were pyrolyzed into a carbon particle cloud around the Ni foams at 800 °C for 1 h under vacuum with a heating rate of 5 °C min^{-1} and cooled down to room temperature at the rate of -5 °C min^{-1}.

2.2. Synthesis of the CdS@NG electrode

First, 1 mmol of $C_4H_6CdO_4 \cdot 2H_2O$, 1 mmol of $CS(NH_2)_2$ and 0.1 g of PVP-K30 were dissolved in 20 ml of glycerol. Subsequently, the solution was transferred to a 100 ml Teflon-lined stainless-steel autoclave with NG-supported Ni foams immersed in the reaction solution. The autoclave was sealed

and maintained at 180 °C for 6 h. After cooling to room temperature, the CdS@NG electrodes were washed with deionized water and dried in a vacuum oven at 120 °C.

2.3. Synthesis of the MnO_2-CdS@NG electrode

First, 1 mmol of $C_4H_6MnO_4 \cdot 4H_2O$ was dissolved in 20 ml of glycerol, and then the solution was transferred to a 100 ml Teflon-lined stainless-steel autoclave with CdS@NG electrodes immersed in the reaction solution. After left to sit for 10 h, the autoclave was sealed and maintained at 180 °C for 1 h. After cooling to room temperature, the MnO_2-CdS@NG electrodes were washed with deionized water and dried in a vacuum oven at 120 °C.

2.4. Structure characterization and electrochemical evaluation

The surface morphology and elemental distribution were observed by scanning electron microscopy-energy dispersive spectroscopy (SEM-EDS) using a ZEISS Merlin Compact spectroscope (ZEISS, Germany). The microstructure was examined by transmission electron microscopy (TEM), using a JEM-2100F (JEM, Japan). X-ray diffraction (XRD) patterns were recorded by a D8 advance diffractometer (Bruker, Germany). Raman spectroscopy was recorded with an inVia Raman microscope (Renishaw, UK).

Cyclic voltammetry (CV), galvanostatic charge-discharge (GCD) and electrochemical impedance spectroscopy (EIS) were performed by using a three-electrode system in 6 M KOH electrolyte solution with an AUTOLAB-AUT86742 (Wantong, Switzerland). The counter electrode, reference electrode and working electrode were a platinum plate, Hg/HgO electrode and MnO_2-CdS@NG electrode, respectively.

The specific capacitance can be calculated from the discharge curves using the following equation:

$$C_{sp} = \frac{I \times \Delta t}{m \times \Delta V}$$

where C_{sp}, I, Δt, m and ΔV are the specific capacitance (F g^{-1}), discharge current (A), discharge time (s), mass of the active material (g) and potential window (V), respectively.

The asymmetric supercapacitor was fabricated using MnO_2-CdS@NG as a positive electrode and rGO as a negative electrode. The mass ratio of MnO_2-CdS@NG and rGO can be roughly calculated from the following formula:

$$\frac{m_+}{m_-} = \frac{C_{S-} \times \Delta V_-}{C_{S+} \times \Delta V_+}$$

where m is the mass (g), C_s is the specific capacitance (F g^{-1}), and the ΔV is the potential window (V) of each electrode. The mass ratio of MnO_2-CdS@NG and rGO is approximately 0.3, according to the calculated formula. The MnO_2-CdS@NG//rGO asymmetric supercapacitor was investigated in a 6 M KOH electrolyte to demonstrate its practical application in energy storage.

The energy density and power density of the MnO_2-CdS@NG//rGO asymmetric supercapacitor were calculated by the following equation:

$$E_m = \frac{C_{SP} \times \Delta V^2}{2 \times 3.6}$$

$$P_m = \frac{E_m \times 3600}{t_{dis}}$$

where E_m and P_m are the energy density (W h kg^{-1}) and power density (W kg^{-1}), respectively. ΔV is the potential window (V) of the MnO$_2$-CdS@NG//rGO asymmetric supercapacitor, and t_{dis} is the discharge time (s).

3. RESULTS AND DISCUSSION

3.1. Morphological analysis

Fig. 1a and 1b show the surface morphology of the pure Ni matrix and the Ni matrix covered by N-doped graphite (NG) layer, respectively. Clearly, the NG layer combines tightly and uniformly to the Ni matrix with many pores distributed on the surface. Fig. 1c shows the morphology of the MnO$_2$-CdS@NG electrode, and Fig. 1d is a detailed image of the special structure that MnO$_2$ nanowires penetrate the gaps between these CdS agglomerated particles.

To further observe the microstructure, TEM images were captured and are shown in Fig. 1e and 1f. An apparent MnO$_2$ nanowire can be observed, which is surrounded by a mass of ultrafine CdS nanoparticles. The marginal area with a wrinkled structure is the graphene-based exfoliation from the NG layer. The lattice fringe of the nanoparticle with an interplanar distance of 0.33 nm corresponds to the (1 1 1) plane of CdS. These SEM and TEM images demonstrate that these MnO$_2$ nanowires act as a strengthening phase that can tightly anchor CdS on the electrode surface.
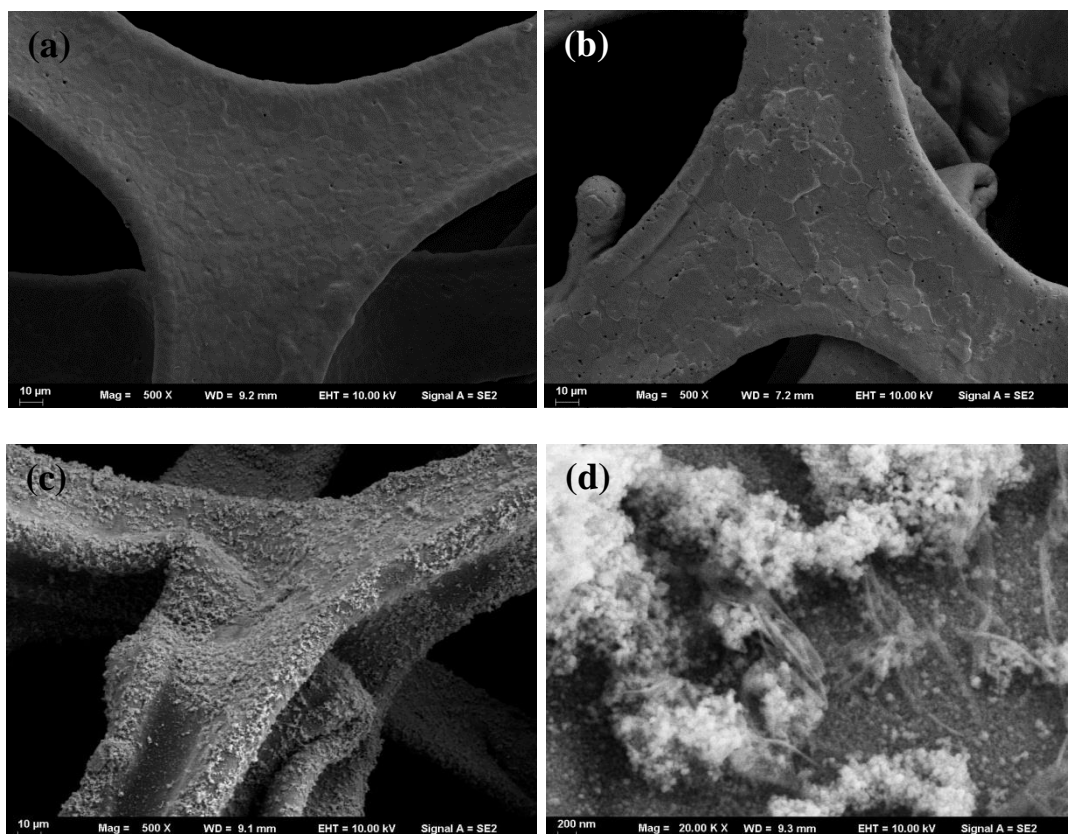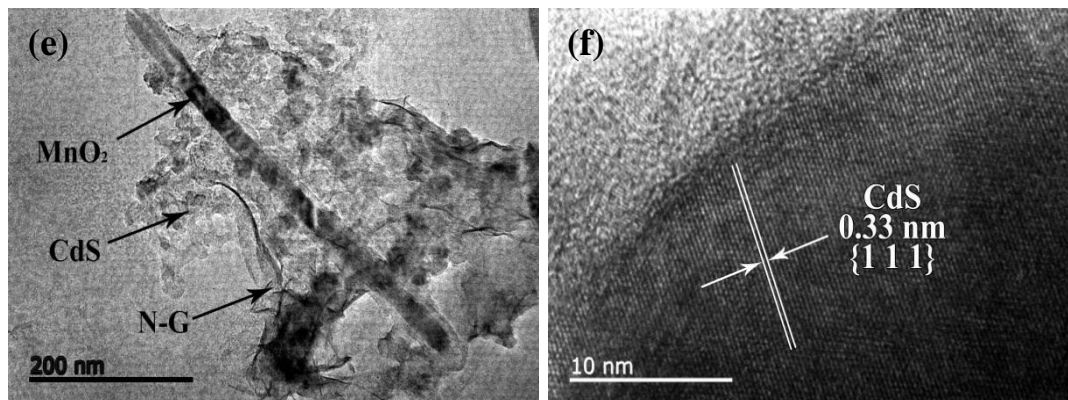
Figure 1. FE-SEM images of (a) the Ni matrix, (b) the Ni matrix covered by an NG layer, (c) the morphology of the MnO_2-CdS@NG electrode, (d) detailed image; (e) TEM image of MnO_2-CdS@NG structure, (f) high-resolution TEM image of CdS.

3.2. Elemental composition and structural characterization

To further investigate the structure of the NG layer, Raman spectroscopy was performed and is shown in Fig. 2a. Two apparent Raman peaks, which represent the disordered sp3 carbon atoms (D band at 1378 cm^{-1}) and the stable sp2 carbon atoms (G band at 1594 cm^{-1}) can be obviously observed. In addition, the broad Raman peak at approximately 2800 cm^{-1} is assigned to the G' band, which is characteristic of highly ordered graphitic lattices. The XPS analysis of the N element is shown in Fig. 2b. It is clear that the graphitic-N, pyrrolic-N and pyridinic-N coexist in the NG layer.

Fig. 2c shows the structural transformation of the electrode surface. The lowest curve is assigned to the NG layer. Two apparent peaks at $2\theta = 26.5°$ and $44.5°$ can be observed, which correspond to the (0 0 2) and (1 0 1) planes of graphite (JCPDS card No. 65-6212), respectively. The middle one is assigned to the ultrafine CdS nanoparticles. Three apparent peaks at $2\theta = 26.5°$, $43.9°$ and $52.1°$ correspond to the (1 1 1), (2 2 0) and (3 1 1) planes of CdS (JCPDS card No. 75-1546), respectively. The uppermost curve is assigned to the MnO_2-CdS structure. The extra characteristic peak at $2\theta = 37.0°$ corresponds to the (2 1 1) planes of MnO_2 (JCPDS card No. 53-0633). The Raman spectra of CdS and MnO_2-CdS are shown in Fig. 2d. Two apparent peaks at 302 cm^{-1} and 598 cm^{-1} represent the great crystallinity of CdS [20]. Two low peaks at 483 cm^{-1} and 637 cm^{-1} are assigned to the MnO_2 nanowires [21].

Fig. 2e and 2f illustrate the EDS analysis of the NG layer and MnO_2-CdS@NG electrode. The coexistence of Mn, O, Cd and S demonstrates the MnO_2-CdS composite structure. The excessive content of the O element caused by the solvothermal reaction is a benefit for improving the wettability of the electrode.
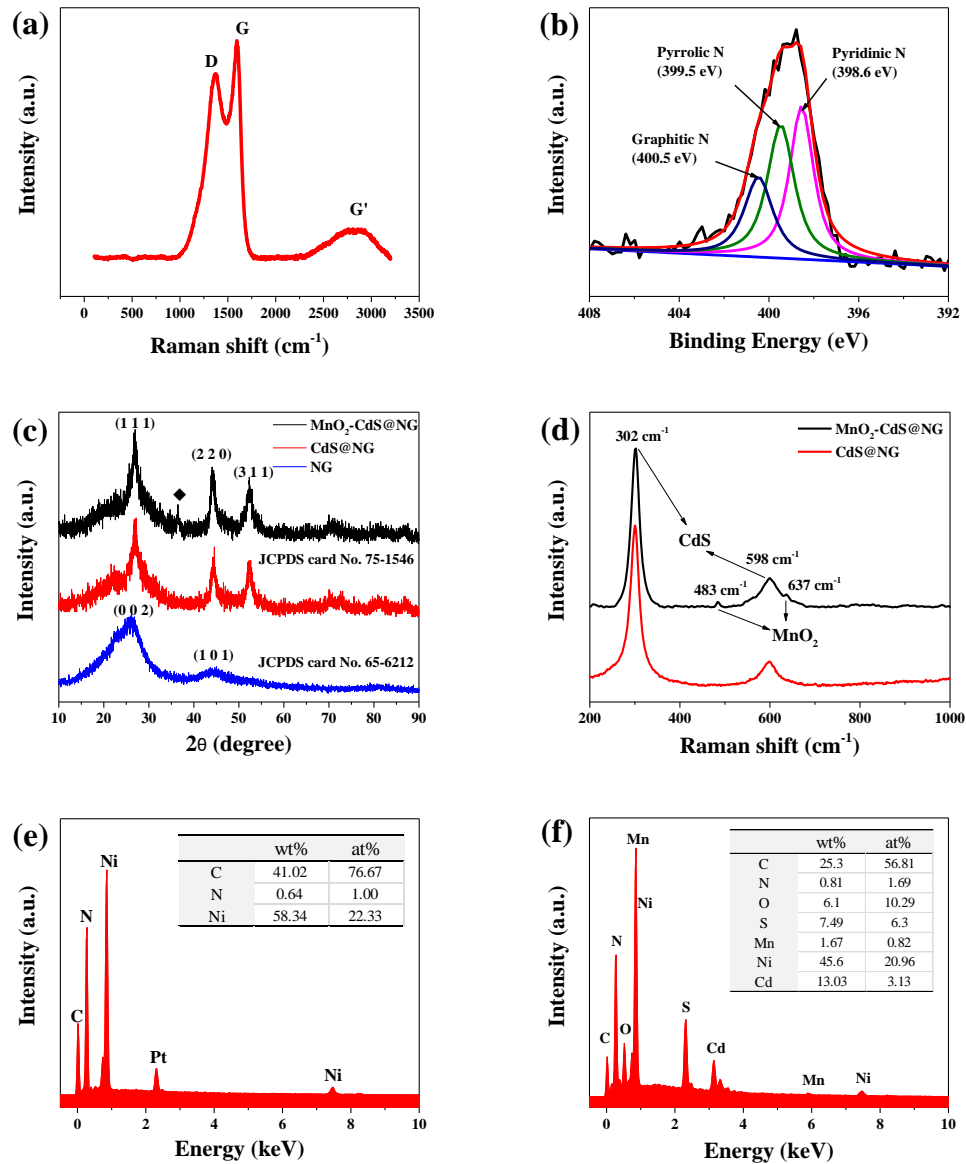
Figure 2. (a) Raman spectra of the NG layer, (b) XPS analysis of the N element, (c) XRD patterns of NG, CdS@NG and MnO_2-CdS@NG, (d) Raman spectra of the CdS@NG and MnO_2-CdS@NG electrode, (e) EDS analysis of the NG layer, (f) EDS analysis of the MnO_2-CdS@NG electrode.

3.3 Electrochemical measurements with three-electrode system

The electrochemical properties of the CdS@NG electrode and MnO_2-CdS@NG electrode were estimated by cyclic voltammetry (CV), galvanostatic charge-discharge (GCD) and electrochemical impedance spectroscopy (EIS) in a 6 M KOH electrolyte solution with a three-electrode system. Fig. 3a illustrates the curves of the CdS@NG electrode and MnO_2-CdS@NG electrode at the same scan rate of 10 mV s^{-1} with a potential window from -0.1 to 0.5 V. A pair of redox peaks can be observed in these curves, which is the typical pseudocapacitive characteristic of supercapacitors. In addition, a new oxidation peak is visible in the CV curve of MnO_2-CdS@NG electrode, which is assigned to the MnO_2

nanowires. The left shift of the peak position demonstrates that the presence of the MnO_2 nanowires facilitated the redox reaction at the MnO_2-CdS@NG electrode. In addition, the CV integral area of the MnO_2-CdS@NG electrode was slightly larger than that of the CdS@NG electrode. Therefore, MnO_2-CdS@NG electrode naturally exhibited a higher specific capacitance. Fig. 3b illustrates the CV curves of the MnO_2-CdS@NG electrode at different scan rates from 5 to 50 mV s^{-1}. With an increase in the scan rate, the rapid increase in the peak current and the small shift in the position demonstrate the rapid reaction kinetics of the electrode.
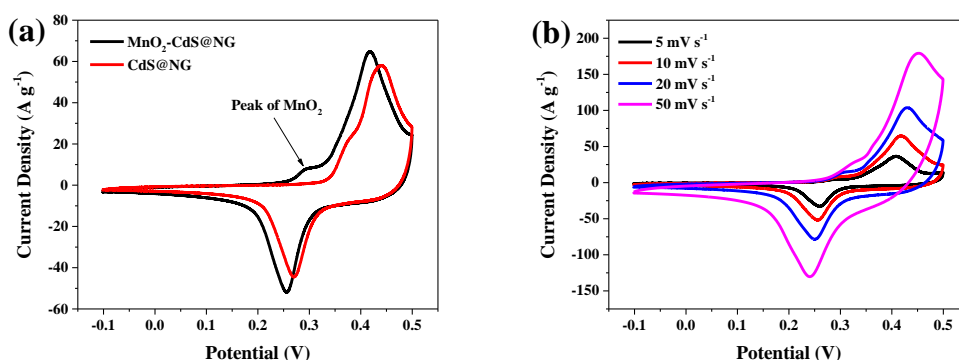

Figure 3. (a) CV curves of the CdS@NG and MnO_2-CdS@NG electrode at a scan rate of 10 mV s^{-1}, (b) CV curves of the MnO_2-CdS@NG electrode at different scan rates from 5 to 50 mV s^{-1}.

Galvanostatic charge-discharge (GCD) measurements were carried out at various current densities from 2 to 50 A g^{-1} with a potential range from -0.1 to 0.45 V. Fig. 4a and 4b illustrates the GCD curves of the CdS@NG electrode and MnO_2-CdS@NG electrode. The nonlinear shape of the GCD curves is mainly attributed to the reversible redox reactions of the Cd^+/Cd^{2+} couple associated with OH^-, which is consistent with the CV results. As shown in Fig. 4c, the specific capacitance can be calculated through the GCD curves of the CdS@NG and MnO_2-CdS@NG electrodes. At discharge current densities of 2, 5, 10, 20, 30, 40 and 50 A g^{-1}, the specific capacitance of the CdS@NG electrode was 1247, 1021, 896, 793, 727, 662 and 607 F g^{-1}, respectively. The calculated value was higher than that of CdS synthesized directly on the Ni matrix. It can be attributed to the N element doped in the graphite structure, which increases the atomic charge density and causes asymmetry in the spin density of the carbon network. That facilitates the charge transfer from the current collector to the active material and causes a more efficient redox reaction [22-28]. Significantly, the specific capacitance of the MnO_2-CdS@NG electrode at the same discharge current densities were 1497, 1241, 1095, 985, 913, 865 and 812 F g^{-1}, which can be attributed to further activation resulting from the MnO_2 nanowires. The penetrating MnO_2 nanowires prompted charge transfer into the interior of the CdS, which allowed a more efficient redox reaction. In addition, the MnO_2-CdS@NG electrode exhibited a higher retention at 54.2% (1497 to 812 F g^{-1}) than the CdS@NG electrode at 48.7% (1247 to 607 F g^{-1}).

EIS analysis was performed to investigate the charge transfer kinetics at the interface of the electrode and electrolyte. Fig. 4d illustrates the Nyquist plots of the NG electrode, CdS@NG electrode and MnO_2-CdS@NG electrode, respectively. These curves, with an approximate 90° phase angle, reveal the typical capacitor behaviour [29-31]. The inset illustrates the difference at high frequencies,

which is associated with the charge-transfer resistance. It is clear that the NG electrode possesses almost no charge-transfer resistance. However, the CdS@NG electrode and MnO$_2$-CdS@NG electrode exhibit a similar weak retardation, revealing that the NG layer is an ideal interlayer between the electrode active materials and the Ni matrix, which not only provides active sites but also reveals a high conductivity. In addition, the low charge-transfer resistance of CdS@NG electrode and MnO$_2$-CdS@NG electrode (less than 1Ω) ensure the rapid charge exchange at the interface of the electrode and electrolyte.
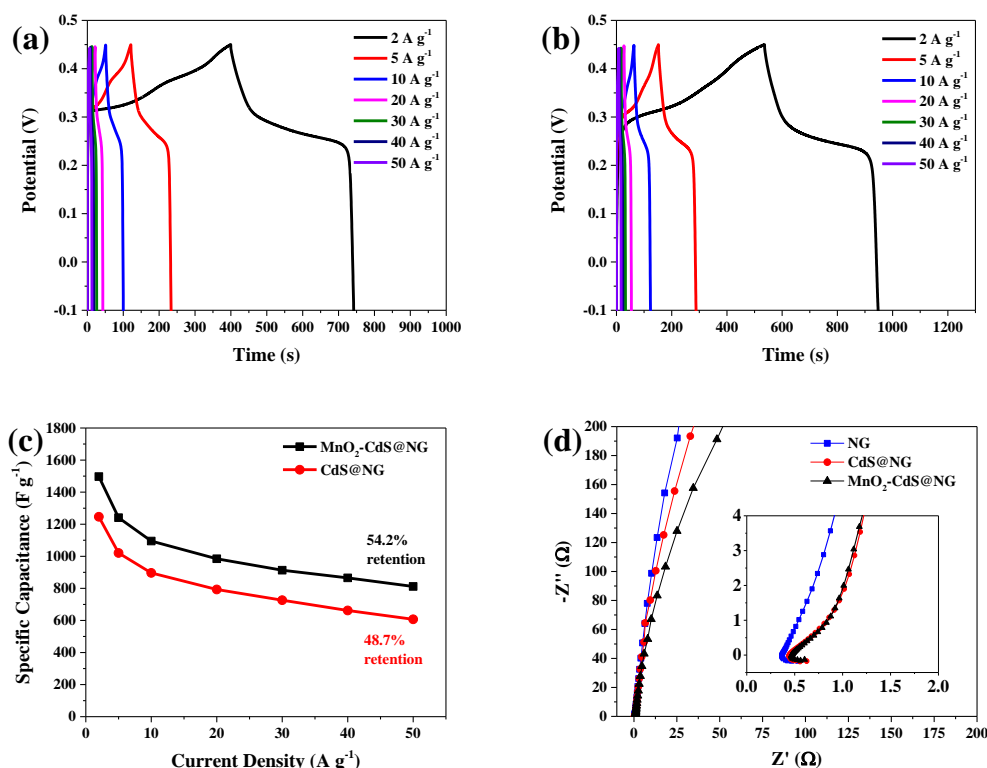

Figure 4. (a) GCD curves of the CdS@NG electrode, (b) GCD curves of the MnO$_2$-CdS@NG electrode, (c) specific capacitance of the CdS@NG and MnO$_2$-CdS@NG electrode at different current densities, (d) EIS Nyquist plots.

Since SCs have superior high power output, the high-rate stability and reversibility are important parameters for their practical applications. Fig. 5a exhibits the continuous GCD measurements of the CdS@NG electrode and the MnO$_2$-CdS@NG electrode at a changing current density from 10 to 50 A g^{-1}. After the high-rate continuous GCD measurement for 300 cycles, the specific capacitance of the CdS@NG electrode decreased by 23.5%; however, the MnO$_2$-CdS@NG electrode specific capacitance decreased by only 10.3%. In addition, Fig. 5b shows the continuous GCD measurements of the CdS@NG electrode and MnO$_2$-CdS@NG electrode at a current density of 20 A g^{-1} for 500 cycles. The capacitance retention was 54.5% and 74.6%, respectively. The integral area of the MnO$_2$-CdS@NG electrode decay curve was 39.3% larger than that of the CdS@NG electrode, which reveals the enhanced performance of the MnO$_2$-CdS@NG electrode. The improved cycling stability of the MnO$_2$-CdS@NG electrode benefits from the anchoring and conduction effect of the MnO$_2$ nanowires, by avoiding exfoliation during high-rate charge-discharge processes.
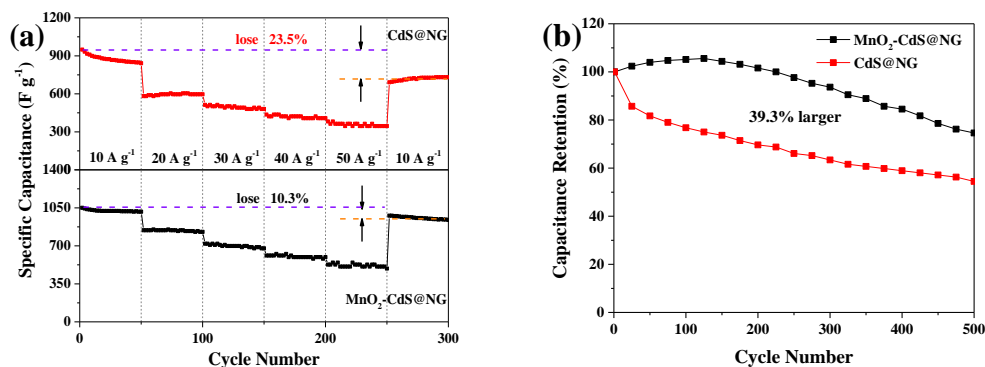
Figure 5. (a) The rate stability and (b) high-rate cyclic stability of the CdS@NG and MnO$_2$-CdS@NG electrode.

In view of these above characterizations and electrochemical measurements, the high performance of the MnO$_2$-CdS@NG electrode can be attributed to the following points. First, N doping in the NG interlayer facilitates the charge transfer between the current collector and the active material. Second, the ultrafine nanoparticle morphology of CdS provides a large specific area for effective contact with the electrolyte. Third, the MnO$_2$ nanowires penetrating the CdS agglomerated particles can be regarded as the strengthening phase, which anchors the CdS on the surface of the electrode, prompting charge transfer into the interior of the CdS and facilitating a more efficient redox reaction. Compared with the recent studies, as shown in Table 1, the MnO$_2$-CdS@NG electrode exhibits the superior electrochemical performance.

Table 1. Comparative representation of the specific capacity of recently reported CdS-based, MnO$_2$-based and N-doped carbon electrode active materials.

Electrode	Specific capacitance	Reference
Porous CdS@Ni foam	909 F g^{-1} at 2 mA cm^{-2}	[11]
3D CdS@rGO	300 F g^{-1} at 5 mV s^{-1}	[12]
3D porous N-doped carbon aerogel	255 F g^{-1} at 0.5 A g^{-1}	[32]
MnO$_2$@carbon fibres	228 F g^{-1} at 1 A g^{-1}	[33]
MnO$_2$@3D porous carbon skeleton	386 F g^{-1} at 1 A g^{-1}	[34]
CoS@graphitic carbon nitride	668 F g^{-1} at 2 A g^{-1}	[35]
CdS@NG	1247 F g^{-1} at 2 A g^{-1}	This work
MnO$_2$-CdS@NG	1497 F g^{-1} at 2 A g^{-1}	This work

3.4 Electrochemical measurements of the MnO$_2$-CdS@NG//rGO asymmetric supercapacitor

To evaluate the practical energy storage applications of the MnO$_2$-CdS@NG electrode, rGO was used as a negative electrode to assemble the asymmetric supercapacitor. Fig. 6a shows the CV curves of the MnO$_2$-CdS@NG and rGO electrode at the scan rate of 5 mV s^{-1}. In consideration of the charge balance, the mass ratio of the MnO$_2$-CdS@NG and rGO is approximately 0.3. The MnO$_2$-CdS@NG//rGO asymmetric supercapacitor was investigated by CV and GCD measurement in a 6 M KOH electrolyte solution. Fig. 6b illustrates the CV curves of the MnO$_2$-CdS@NG//rGO at different

scan rates from 5 to 50 mV s^{-1} with a potential window from 0 to 1.6 V. The great shape retention of the CV curves demonstrates the rapid reaction kinetics of the electrode. GCD measurements were performed at different current densities from 1 to 20 A g^{-1}. The GCD curves are shown in Fig. 6c, and the specific capacitance was 101, 87, 71, 58 and 42 F g^{-1}, shown in Fig. 6d, respectively.
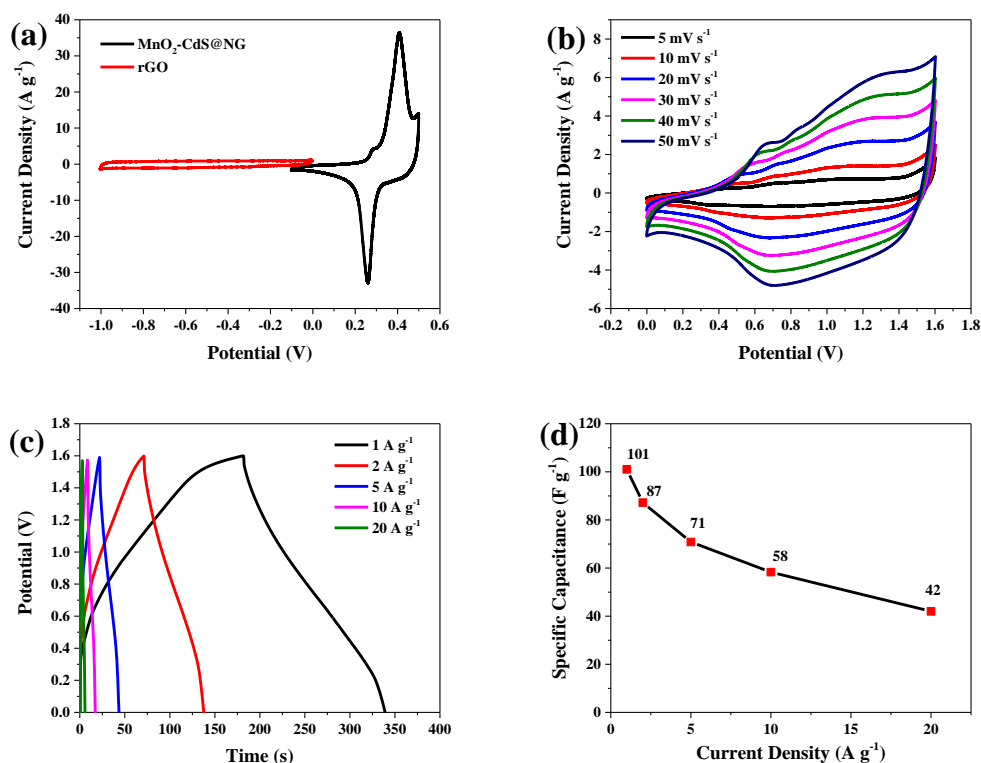

Figure 6. (a) CV curves of the MnO$_2$-CdS@NG and rGO electrode at the scan rate of 5 mV s^{-1}, (b) CV curves of the MnO$_2$-CdS@NG//rGO asymmetric supercapacitor at different scan rates from 5 to 50 mV s^{-1}, (c) GCD curves of the MnO$_2$-CdS@NG//rGO asymmetric supercapacitor at different current densities from 1 to 20 A g^{-1}, (d) specific capacitance at different current densities.

Fig. 7a illustrates the capacitance retention curve after the continuous GCD measurement at a current density of 10 A g^{-1} for 5000 cycles. The retention rate is 87%, which demonstrates the high cycling stability of the MnO$_2$-CdS@NG//rGO asymmetric supercapacitor. A Ragone plot related to the energy and power densities was created and is shown in Fig. 7b. The energy density can reach up to 33.8 W h kg^{-1} at a power density of 776 W kg^{-1}, which is higher than the value from other recent studies, as show in Table 2. These high performances of the MnO$_2$-CdS@NG//rGO asymmetric supercapacitor demonstrate the promising applications of this novel device.
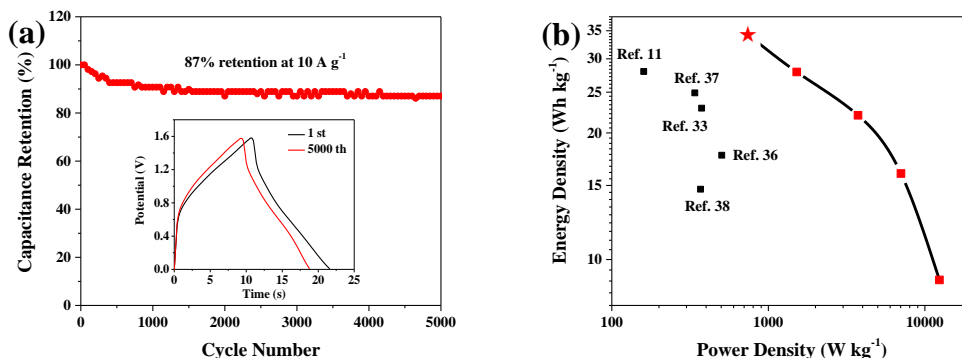
Figure 7. (a) Cyclic stability, (b) Ragone plots of MnO_2-CdS@NG//rGO asymmetric supercapacitor.

Table 2. Comparative representation of the energy density with recently reported asymmetric supercapacitors.

Asymmetric supercapacitor	Energy density	Reference
Porous CdS@Ni foam // AC	28.0 Wh kg^{-1} at 160 W kg^{-1}	[11]
MnO_2@carbon fibres // AC	22.9 Wh kg^{-1} at 375 W kg^{-1}	[33]
CuS network // AC	17.7 Wh kg^{-1} at 504 W kg^{-1}	[36]
$NiCo_2S_4$ nanotube // rGO	24.9 Wh kg^{-1} at 339 W kg^{-1}	[37]
CoSx//rGO	14.7 Wh kg^{-1} at 369 W kg^{-1}	[38]
MnO_2-CdS@NG // rGO	33.8 Wh kg^{-1} at 776 W kg^{-1}	This work

The superior electrochemical performance of the MnO_2-CdS@NG//rGO asymmetric supercapacitor can be attributed to the following synergies. First, the appropriate mass ratio of the anode and cathode active materials ensured the balance of the charge transfer, which can effectively avoid the polarization of the electrodes. Second, the MnO_2 nanowires penetrating the CdS particles facilitated a more efficient redox reaction at the interior active material. Third, the connection of a pseudocapacitive electrode (MnO_2-CdS@NG electrode) and an electrical double-layer capacitor (rGO) is an effective method to prolong the cycling stability.

4. CONCLUSIONS

For the first time, a MnO_2-CdS@NG electrode was synthesized by a two-step solvothermal method. The MnO_2 nanowires acted as a strengthening phase by penetrating the gaps between the CdS particles and tightly anchoring them on the surface of NG. It is clear that the presence of the MnO_2 nanowires prompted charge transfer into the interior CdS and facilitated the redox reaction at the MnO_2-CdS@NG electrode. Due to the synergy of the N-doped interlayer and the novel reinforced structure, the charge transfer between the current collector and the active materials was accelerated. From the electrochemical measurements, the specific capacitance of the MnO_2-CdS@NG electrode was 1497 F g^{-1} at a current density of 2 A g^{-1}. In addition, the MnO_2-CdS@NG//rGO asymmetric supercapacitor exhibited a superior energy density (33.8 W h kg^{-1} at a power density of 776 W kg^{-1})

and a great cycling stability (87% at a current density of 10 A g^{-1} for 5000 cycles). In summary, this work demonstrates the practical application of a MnO_2-CdS@NG electrode for SCs, and the novel structure can be regarded as a promising approach to improve the performance of other active materials.

References

1. L. Dong, C. Xu, Y. Li, Z. H. Huang, F. Kang, Q.-H. Yang and X. Zhao, *J. Mater. Chem. A*, 4 (2016) 4659.
2. L. Mao, Q. Meng, A. Ahmad and Z. Wei, *Adv. Energy Mater.*, (2017) 1700535.
3. J. Wen, X. Zhang and H. Gao, *Phys.Chem.Chem.Phys.*, 19 (2017) 9509.
4. L. Borchardt, M. Oschatz and S. Kaskel, *Chem. Eur. J.*, 22(2016) 7324.
5. S. Li, C. Yu, J. Yang, C. Zhao, M. Zhang, H. Huang, Z. Liu, W. Guo and J. Qiu, *Energy Environ. Sci.*, 10 (2017) 1958.
6. L. Yang, H. Li, H. Liu and Y. Zhang, *Int. J. Electrochem. Sci.*, 12 (2017) 1.
7. P. Simon and Y. Gogotsi, *Nat. Mater.*, 7 (2008) 845.
8. Y. P. Gao and K. J. Huang, *Chem. Asian J.*, 12 (2017) 1969.
9. M. Guo, J. Balamurugan, T. D. Thanh, N. H. Kim and J. H. Lee, *J. Mater. Chem. A*, 4 (2016) 17560.
10. G. C. Li, M. Liu, M. K. Wu, P. F. Liu, Z. Zhou, S. R. Zhu, R. Liu and L. Han, *RSC Adv.*, 6 (2016) 103517.
11. P. Xu, J. Liu, P. Yan, C. Miao, K. Ye, K. Cheng, J. Yin, D. Cao, K. Li and G. Wang, *J. Mater. Chem. A*, 4 (2016) 4920.
12. X. Zhang, X. Ge, S. Sun, Y. Qu, W. Chi, C. Chen and W. Lu, *CrystEngComm*, 18 (2016) 1090.
13. Y. Wang, Y. Ma, G. Z. Guo, Y. Zhou, Y. Zhang, Y. Sun and Y. Liu, *Int. J. Electrochem. Sci.*, 12 (2017) 2135.
14. Z. Ma, X. Huang, S. Dou, J. Wu and S. Wang, *J. Phys. Chem. C*, 118 (2014) 17231.
15. X. Ou, L. Gan and Z. Luo, *J. Mater. Chem. A*, 2 (2014) 19214.
16. C. Prehal, C. Koczwara, N. Jäckel, A. Schreiber, M. Burian, H. Amenitsch, M. A. Hartmann, V. Presser and O. Paris, *Nat. Energy*, 2 (2017) 16215.
17. H. Sun, L. Mei, J. Liang, Z. Zhao, C. Lee, H. Fei, M. Ding, J. Lau, M. Li, C. Wang, X. Xu, G. Hao, B. Papandrea, I. Shakir, B. Dunn, Y. Huang and X. Duan, *Science*, 356 (2017) 599.
18. Z. Sun, X. Cai, Y. Song and X. X. Liu, *J. Power Sources*, 359 (2017) 57.
19. T. Yuan, W. T. Li, W. Zhang, Y. S. He, C. Zhang, X. Z. Liao and Z. F. Ma, *Ind. Eng. Chem. Res.*, 53 (2014) 10849.
20. S. Han, Y. C. Pu, L. Zheng, J. Z. Zhang and X. Fang, *J. Mater. Chem. A*, 3 (2015) 22627.
21. C. Tanggarnjanavalukul, N. Phattharasupakun, K. Kongpatpanich and M. Sawangphruk, *Nanoscale*, 9 (2017) 13630.
22. D. Geng, Y. Chen, Y. Chen, Y. Li, R. Li, X. Sun, S. Ye and S. Knights, *Energy Environ. Sci.*, 4 (2011) 760.
23. T. Lin, I. W. Chen, F. Liu, C. Yang, H. Bi, F. Xu and F. Huang, *Science*, 350 (2015) 1508.
24. J. P. Paraknowitsch and A. Thomas, *Energy Environ. Sci.*, 6 (2013) 2839.

25. C. Tang, Y. Liu, D. Yang, M. Yang and H. Li, *Carbon*, 122 (2017) 538.
26. B. P. Vinayan, R. Nagar, N. Rajalakshmi and S. Ramaprabhu, *Adv. Funct. Mater.*, 22 (2012) 3519.
27. X. Wang, G. Sun, P. Routh, D. H. Kim, W. Huang and P. Chen, *Chem. Soc. Rev.*, 43 (2014) 7067.
28. Y. Zhao, S. Huang, M. Xia, S. Rehman, S. Mu, Z. Kou, Z. Zhang, Z. Chen, F. Gao and Y. Hou, *Nano Energy*, 28 (2016) 346.
29. V. Augustyn, J. Come, M. A. Lowe, J. W. Kim, P.-L. Taberna, S. H. Tolbert, H. D. Abruña, P. Simon and B. Dunn, *Nat. Mater.*, 12 (2013) 518.
30. V. Augustyn, P. Simon and B. Dunn, *Energy Environ. Sci.*, 7 (2014) 1597.
31. M. R. Lukatskaya, B. Dunn and Y. Gogotsi, *Nat. Commun.*, 7 (2016) 12647.
32. Y. Hu, X. Tong, H. Zhuo, L. Zhong, X. Peng, S. Wang and R. Sun, *RSC Adv.*, 6 (2016) 15788.
33. C. Zhao, Z. Ge, Y. Zhou, Y. Huang, G. Wang and X. Qian , *Carbon*, 114 (2017) 230.
34. X. Luo, J. Yang, D. Yan, W. Wang, X. Wu and Z. Zhu, *J. Alloy. Compd.*, 723 (2017) 505.
35. D. Jiang, Q. Xu, S. Meng, C. Xia and M. Chen, *J. Alloy. Compd.*, 706 (2017) 41.
36. W. Fu, W. Han, H. Zha, J. Mei, Y. Li, Z. Zhang and E. Xie, *Phys. Chem. Chem. Phys.* 18 (2016) 24471.
37. H. Chen, S. Chen, H. Shao, C. Li, M. Fan, D. Chen, G. Tian and K. Shu, *Chem. Asian J.*, 11 (2016) 248.
38. D.P. Dubal, G.S. Gund, C.D. Lokhande and R. Holze, *Energy Technol.*, 2 (2014) 401.